Proceedings of the ASME 2010 3rd Joint US-European Fluids Engineering Summer Meeting and 8th International Conference on Nanochannels, Microchannels, and Minichannels
FEDSM-ICNMM2010
August 1-5, 2010, Montreal, Canada

FEDSM-ICNMM2010-30968

TRANSIENT SIMULATIONS OF 3-D SUPERSONIC MICRONOZZLE FLOW

W.L. Louisos
School of Engineering
University of Vermont
Burlington, Vermont 05405
Email: william.louisos@uvm.edu

Darren L. Hitt
School of Engineering
University of Vermont
Burlington, Vermont 05405
Email: darren.hitt@uvm.edu

ABSTRACT

A numerical investigation of transient performance of $3D$ *linear micronozzles has been performed. The baseline model for the study is derived from the NASA/Goddard Space Flight Center MEMS-based hydrogen peroxide micro-thruster prototype. The* $3D$ *micronozzles investigated here have depths of* $25\mu m$, $50\mu m$, $100\mu m$, *and* $150\mu m$ *and employ expanders with a* 30° *half-angle. A hyperbolic-tangent actuation profile is used to model the opening of a microvalve in order to simulate start-up of the thruster. The inlet stagnation pressure when the valve is fully opened is* $250kPa$ *and generates a maximum throat Reynolds number of* $Re_{max} \sim 800$*. The complete actuation occurs over* $0.55ms$ *and is followed by* $0.25ms$ *of steady-state operation. The propulsion scheme employs* 85% *pure hydrogen peroxide as a monopropellant. Simulation results have been analyzed and thrust production as a function of time has been quantified along with the total impulse delivered. Micronozzle impulse efficiency has also been determined based on a theoretical maximum impulse achieved by a quasi-*$1D$ *inviscid flow responding instantaneously to the actuation profile. It is found that both the flow and thrust exhibit a response 'lag' to the time-varying inlet pressure profile. Simulations are compared to previous* $2D$ *results and indicate that thrust per unit nozzle depth, impulse, and efficiency increase with nozzle depth and approach the* $2D$ *results for nozzle depths greater than* $150\mu m$*.*

NOMENCLATURE

A area $\left(m^2\right)$
$\mathbf{F}$ thrust (N)
g gravity $\left(m/s^2\right)$
I impulse $\left(\frac{N\cdot s}{m}\right)$
L characteristic length scale (m)
$\dot{m}$ mass flow rate (kg/s)
p pressure (Pa)
R gas constant $\left(\frac{J}{kgK}\right)$
Re Reynolds number
T static temperature (K)
t time (s)
$\mathbf{u}$ velocity (m/s)
γ ratio of specific heats
η nozzle impulse efficiency $(\%)$
θ expander half-angle (deg)
μ viscosity $\left(\frac{kg}{m^2\cdot s}\right)$
ρ density $\left(kg/m^3\right)$

Subscripts

$exit$ nozzle exit conditions
f final
i initial
max maximum
0 stagnation condition
∞ ambient condition

Superscripts

$*$ throat condition

INTRODUCTION

The aerospace community is currently pursuing the use of miniaturized satellites for the next generation of space missions. These small scale satellites, commonly referred to as nanosatellites, or 'nanosats,' will be capable of performing formation-flying type orbital patterns. Nanosats require miniaturized propulsion systems able to provide the low levels of thrust and impulse necessary for orbital maneuvering and station-keeping. Micro-Electro-Mechanical-Systems (MEMS) based technologies offer great potential in satisfying the stringent size and energy constraints associated with nanosatellites. A comprehensive discussion of small satellite technologies and technical challenges can be found in the recent monograph by Helvajian and Janson [1].

A key component of the miniaturized propulsion system is the supersonic micronozzle. Upstream of the nozzle inlet, a propellant undergoes combustion and/or chemical decomposition which releases thermal and pressure energy. The role of the supersonic nozzle is to convert this available energy into kinetic energy and thrust. Control of the spacecraft is achieved by applying discrete impulse bits and so the impulse delivered by the micronozzle is a key parameter of interest. The use of quasi-1D theory can lead to errors in performance calculations owing to viscous forces on the micro-scale. It is possible that impulse shortages can result from a viscous 'delay' in flow response to transient inlet conditions or if micronozzle expander angles are made too large when attempting to compensate for viscous effects. The relationship between viscous forces and geometric losses represents an inherent trade-off in micronozzle flows.

It is well documented in the literature that viscous forces play a significant role in determining the micronozzle flow-field and performance characteristics. Owing to the reduced size, the supersonic flow remains laminar ($Re < 1,000$) and viscous forces generate subsonic 'boundary' layers along the nozzle walls. In an actual $3D$ micronozzle, viscous losses become more pronounced owing to the additional solid wall boundaries and corner effects. These subsonic layers can occupy a significant portion of the expander flow field; up to 100% in certain configurations. This measurably reduces thrust production and performance. It has been shown that subsonic layers on opposing walls can merge in the center of the flow for sufficiently shallow nozzles or low Reynolds numbers. As such, the depth of the device in $3D$ plays an important role.

Viscous effects in supersonic micronozzle flow was first investigated by Bayt and Breuer [2], [3] who demonstrated that the subsonic layer can occupy a significant fraction of the expander flow-field, reducing flow and resulting in thrust loss. Alexeenko *et al.* [4]- [10] have performed extensive DSMC simulations of micronozzle flow for cold gas thrusters with $2D$ axisymmetric and, to a lesser degree, $3D$ geometries. All of the published work has primarily dealt with steady-state, cold-gas flows and limited nozzle geometries have been considered. As the operation of a micro-thruster firing is an inherently transient operation resulting from its intended role of spacecraft attitude adjustment, this is an important consideration and the flow and thrust response on the micro-scale needs to be delineated. The premise is that viscous forces introduce an additional time scale separate from the external time scale of the thruster firing (e.g., valve opening and closing). As such, there is a potential for a lag in thrust production and a discrepancy between the ideal and actual thrust profiles and impulse delivered during a firing. The only studies to consider transient flows include our preliminary work from 2006 [11], the conference paper by Kujawa and Hitt [12], and the paper by Morinigo *et al*. [13]. Morinigo uses an continuum based model to investigate viscous heating of the nozzle substrate during a single rocket firing with hot and cold N_2 gas as the working fluid. The primary limitation of this work is that it examines only a single axis-symmetric nozzle geometry. In this regard, our current study nicely complements and extends the existing micronozzle literature through examination of monopropellant based $3D$ MEMS nozzles with varying etching depths.

The focus of this study is to characterize $3D$ micronozzle flow response and performance during transient operation. Our simulations are based on the hydrogen-peroxide monopropellant micropropulsion scheme and the nozzle geometry is derived from the MEMS-based, NASA/Goddard Space Flight Center prototype microthruster [14]. A typical firing of the thruster (duty cycle) is achieved by the opening and closing of a microvalve which allows the pressurized fuel to flow from a plenum into the catalyst chamber (where the fuel undergoes chemical decomposition) before the gaseous products enter the converging-diverging supersonic micro-thruster nozzle. Over the past 20 years significant progress has been made in the development of micro-scale valves and actuation mechanisms. However, this component of the micro-thruster continues to be an active area of research and development as there are many desirable improvements to be made in the performance of existing microvalves. In fact, microvalves represent a significant hurdle in the successful miniaturization of micro-fluidic systems [15].

Unfortunately, pressure and mass flow rate profiles have not been well characterized for microvalves. As such, valve actuation time is based upon current microvalve prototypes and we make a reasonable estimate of the nozzle inlet pressure profile for the purpose of this transient micronozzle study. A single duty cycle is simulated by changing the nozzle inlet pressure with time to appropriately represent start-up, steady-state, and shut-down of the thruster. The micronozzle inlet pressure is a hyperbolic-tangent profile for the start-up and shut-down segments of the duty cycle which represents typical solenoid valve actuation and is loosely based on the Moog microvalve prototype [16].

In this work, we examine thrust production, impulse, and subsonic layer evolution during start-up, steady-state, and shut-down of the micronozzle duty cycle. This work will bring together key findings from previous studies including viscous losses, transient thrust response, and $3D$ geometric effects. For comparison purposes, results are presented along with previous $2D$ simulations and quasi-1D flow approximations.

MODEL FOR H2O2 MONOPROPELLANT

In this study, we focus our attention on the performance of monopropellant-based micro-thrusters. In particular, we consider decomposed high purity (85%) hydrogen peroxide (H_2O_2) as a potential monopropellant. A monopropellant scheme is attractive for micro-propulsion owing to the relatively high energy density and simplicity of implementation. Hydrogen peroxide is considered a 'green' monopropellant and has been chosen for the development process based on its non-toxicity and relative ease of handling. Decomposition of the H_2O_2 monopropellant occurs in a catalytic chamber upstream of the nozzle inlet according to the one-step reaction

$$2H_2O_2(l) \rightarrow 2H_2O(g) + O_2(g) + heat \qquad (1)$$

where typically Silver (Ag) or Ruthenium Oxide (RuO_2) is used as a catalyst. Chemical equilibrium and thermodynamic properties of the decomposed monopropellant mixture have been calculated from NASA-Glenn's Chemical Equilibrium and Application program (CEA). The CEA calculates chemical equilibrium product concentrations from a given set of reactants and determines thermodynamic and transport properties for the product mixture. The CEA database includes thermodynamic and transport properties for over $2,000$ species and is widely used by the aerodynamics and thermodynamics community [17]. The decomposed monopropellant has been shown to be a homogeneous, frozen (non-reacting) mixture whose thermophysical properties are determined via a mass weighted average of individual component properties of the decomposed monopropellant [18].

The micronozzle inlet gas temperature is assumed to be that of the fully decomposed adiabatic flame temperature of 85% pure decomposed H_2O_2 $(T_0 = 886K)$. The inlet stagnation pressure as a function of time $(p_0(t))$ is shown in Figure **??** and has been chosen based on a steady-state target thrust level in range of $1 - 20\ \mu N$.

The adiabatic flame temperature, or stagnation temperature T_0, along with the specified stagnation pressure $p_0(t)$ establish the inlet pressure boundary condition for the micronozzle simulations. The corresponding Reynolds number for the flow (typically measured at the micronozzle throat) as a function of time is given by

$$Re(t) \equiv \frac{\dot{m}(t)L}{\mu A} \qquad (2)$$

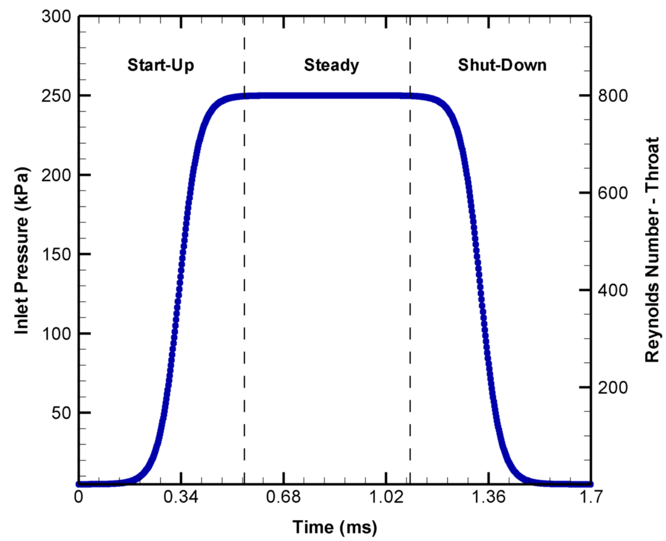

FIGURE 1. The inlet stagnation pressure profile as a function of time imposed on the micronozzle inlet to simulate valve operation. The inlet boundary condition is implemented by means of a User-Defined-Function (UDF). Note that the throat Reynolds number corresponding to the inlet pressure is also shown.

where $\dot{m}$ is the mass flow ratio per unit depth, L is the characteristic length scale (e.g., the $90\mu m$ nozzle throat diameter), μ is the dynamic viscosity of the decomposed monopropellant, and A is the cross sectional area. The value of $\dot{m}$ can be well estimated from quasi-1D theory according to [19]

$$\dot{m}(t) = \frac{p_0(t)A^*}{\sqrt{T_0}}\sqrt{\frac{\gamma}{R}\left(\frac{2}{\gamma+1}\right)^{(\gamma+1)/(\gamma-1)}} \qquad (3)$$

where A^* is the nozzle throat area, γ is the ratio of specific heats, and R is the universal gas constant.

COMPUTATIONAL MODEL

Computational domains are based upon typical nozzle geometries of the micro-thruster prototype developed at NASA/GSFC and described in Ref. [14]. The expander half-angle θ is held constant at $\theta = 30^\circ$ for the $3D$ simulations while the half-angle θ is varied between $10^\circ - 50^\circ$. All other geometric parameters are as shown in Figure 2. Two- and Three-dimensional meshes have been developed using Fluent Inc.'s GAMBIT 2.1 grid generation software. The throat and exit dimensions of the NASA/GSFC prototype (90 μm and 560 μm, respectively) yield an area expansion ratio of $56:9$ and is a

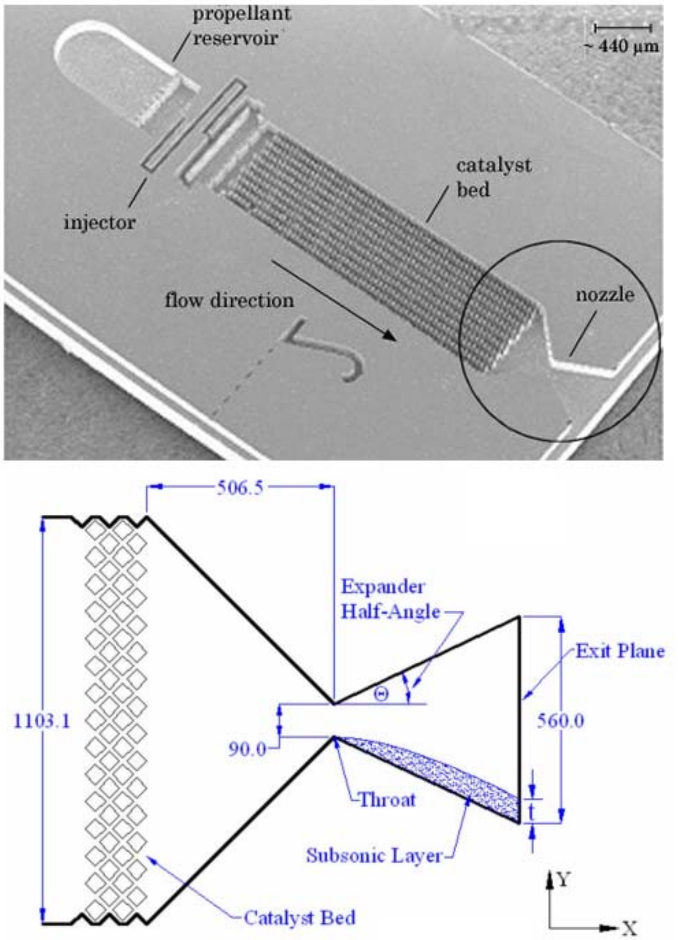

FIGURE 2. An SEM image of the NASA/Goddard and University of Vermont microthruster prototype (top) and the nozzle schematic with relevant dimensions (bottom). Note the size of the subsonic layer at the nozzle exit is denoted by t.

fixed parameter in this study. The mesh varies in size between 1.5×10^6 and 3.5×10^6 total elements depending on the micronozzle etching depth. All mesh elements are quadrilateral with a maximum skewness of 0.5 occurring in less than 4.7% of the elements. Planar symmetry is also utilized in order to reduce computational expenditure. In developing the final meshes, a systematic grid refinement study has been undertaken to ensure that all results are insensitive to further grid refinement. The refinement study examined grid insensitivity at both the low and high ends of the duty cycle Re considered in this study. Thus the computational meshes have been refined to a point where simulations are independent of further grid refinement [20].

Continuum Modeling and Boundary Conditions

A continuum flow model is assumed for the operating conditions of this study. Subsonic portions of the outlet boundaries are prescribed a constant backpressure value of $1.0kPa$. This value serves to maintain the Knudsen number within the continuum regime with the possible exception of some slip regime conditions at the boundaries for the lowest Reynolds numbers considered. For supersonic portions of the domain outlet, the pressure and all other flow quantities are extrapolated from the interior flow via the method of characteristics (Riemann invariants). The flow field in the micronozzle is governed by the conservation equations of mass, momentum, and energy for the fluid mixture according to

$$\frac{\partial}{\partial t}\rho + \nabla \cdot (\rho \mathbf{V}) = 0 \tag{4}$$

$$\frac{\partial}{\partial t}(\rho \mathbf{V}) + \nabla \cdot (\rho \mathbf{V}\mathbf{V}) = -\nabla p + \nabla \cdot (\tau) \tag{5}$$

$$\frac{\partial}{\partial t}(\rho E) + \nabla \cdot (\mathbf{V}(\rho E + p)) = \nabla \cdot (k \nabla T + (\tau \cdot \mathbf{V})) \tag{6}$$

where

$$E = h - \frac{p}{\rho} + \frac{\mathbf{V}^2}{2} \tag{7}$$

$$\tau = \mu \left(\left(\nabla \mathbf{V} + \nabla \mathbf{V}^T \right) - \frac{2}{3} \nabla \cdot \mathbf{V} \mathbf{I} \right) \tag{8}$$

In these equations ρ is the fluid density, $\mathbf{V}$ is the velocity vector, p is the absolute local pressure, E is the total energy, μ is the fluid viscosity, k is the thermal conductivity, T is the static temperature, h is the enthalpy, and τ is the viscous stress tensor. The system of equations is closed by the ideal gas law equation of state

$$p = \rho R T. \tag{9}$$

The micronozzle walls are modeled as no-slip and adiabatic. The operation of a micronozzle as a component in a micropropulsion system is inherently of limited – and often quite short – duration (typically $\ll 1\,$sec). In this work, the entire duty cycle is comprised of $1.7ms$ of flow duration. Furthermore, it will be shown that the flow response time to valve actuation is extremely short and in contrast, the time scale associated with heat transfer through the boundary is substantially longer. Thus it is quite reasonable to regard the process as adiabatic. This notion is further supported by the results in Ref. (e.g., [9]).

Computational Schemes

The inlet boundary condition is a prescribed stagnation pressure $p_0(t)$ that resembles realistic micro-valve actuation [15].

The valve actuation profile is a hyperbolic tangent curve shown in Figure 1. This profile is imposed on the boundary by means of a time-dependant user-defined-function (UDF). A second-order implicit temporal formulation is executed with a step size $\Delta t = 10^{-5}s$. In determining the appropriate time-step size, a systematic approach of successive reductions for Δt has shown that simulations are independent of step size and thus fully resolved in time. We mention here that a coupled-implicit solver is used with a second-order upwind discretization scheme for the convective terms.

The first time step is realized by implementing a steady solution whose initial guess is applied to the domain based on quasi-$1D$ inviscid theory corresponding to $t = 0s$. This solution is allowed to iterate until convergence is achieved and provides a starting point for time advancement. From this, the transient UDF is applied to the inlet boundary according to Figure 1. At each time step, the solution is iterated until it has converged and is then advanced in time. Convergence of the solution at a given time-step is assessed via residuals and monitors for key flow quantities (e.g. $\dot{m}$) at selected locations within the domain. Typically, $5,000$ iterations are required per time-step.

Initially, the valve is closed and there is no pressure gradient across the nozzle and thus no flow. Once the start-up sequence begins, the micro-valve begins to open and a pressure gradient is established across the nozzle which begins to generate a flow. The start-up sequence is defined as the inlet stagnation pressure goes from $0kPa$ to 99% of the steady-state inlet pressure, $p_0\,(steady) = 250kPa$. Start-up occurs for the initial $0.55ms$ of valve actuation. The micronozzle is then operated at steady-state for $0.6ms$ and subsequently the shut-down sequence begins. The entire duty cycle occurs over $1.7ms$ and includes a total of 170 time-steps.

Thrust, Impulse, & Efficiency

In this study we are concerned with evaluating micronozzle performance including thrust production, impulse, and nozzle efficiency for the cases examined. The thrust at any instant in time is formally calculated from the simulation data according to

$$\mathbf{F}(\mathbf{t}) = \int_{A_{exit}} \rho \mathbf{u}\,(\mathbf{u}\cdot\mathbf{n})\,dA + \int_{A_{exit}} (p_{exit} - p_\infty)\,dA \qquad (10)$$

where p_{exit} is the pressure at the exit plane of the nozzle and p_∞ is the ambient backpressure. In our simulations, however, the pressure thrust term is negligible in comparison to the momentum thrust.

The impulse generated for any interval of interest during the duty cycle (firing) of the microthruster is given by

$$\mathbf{I} = \int_{t_i}^{t_f} \mathbf{F}(\mathbf{t})dt \qquad (11)$$

where t_i and t_f are the start and end times of interest. The total impulse for a single duty cycle is found by taking $t_i = 0$ and $t_f = 1.7ms$. With appropriate selection of t_i and t_f the impulse can also be determined for isolated segments of the duty cycle; i.e., the impulse generated during start-up or shutdown.

Another quantity of interest is the impulse efficiency η which can be defined as the ratio of the impulse realized $(\mathbf{I})$ to the maximum possible impulse $(\mathbf{I}_{\max})$ defined by a $1D$ inviscid flow responding *instantaneously* to the valve profile. The impulse efficiency is thus given as

$$\eta = \frac{\mathbf{I}}{\mathbf{I}_{\max}} = \frac{\int_{t_i}^{t_f}\mathbf{F}(\mathbf{t})dt}{\int_{t_i}^{t_f}\mathbf{F}_{\max}(\mathbf{t})dt} \qquad (12)$$

where $\mathbf{F}(\mathbf{t})$ is the thrust production given by Eq. (10) and $\mathbf{F}_{\max}(t)$ is determined from quasi-$1D$ inviscid theory according to

$$\mathbf{F}_{\max}(\mathbf{t}) = \left[\left(\rho_{exit} \times \mathbf{V}_{exit}^2\right) + (p_{exit} - p_\infty)\right] A_{exit} \qquad (13)$$

and $\mathbf{V}_{exit}$ is calculated as

$$\mathbf{V}_{exit} = \frac{p_0 A^*}{\rho_{exit} A_{exit}\sqrt{T_0}} \sqrt{\frac{\gamma}{R}\left(\frac{2}{\gamma+1}\right)^{\left(\frac{\gamma+1}{\gamma-1}\right)}} \qquad (14)$$

with ρ_{exit} and p_{exit} determined from $1D$ isentropic flow relations (e.g., [19]). The calculation for $\mathbf{I}_{\max}$ over the entire duty cycle yields a value of $\sim 0.035\ \mu N\cdot s$ per micron nozzle depth.

NUMERICAL RESULTS

In this section, we first present $2D$ simulation results for varying expander half-angles ranging from $10^\circ - 50^\circ$ as a starting point. Thrust profiles as a function of time are presented along with total impulse and impulse efficiency. Next, we turn to $3D$ simulations and orient the reader with illustrations of $3D$ Mach contours and transient subsonic layers. The $3D$ thrust profiles as a function of time are then presented. Finally, total impulse and efficiency are presented for the micronozzle depth.

2D Flow Response & Thrust Profiles

An illustrative example of the unsteady flow-field response is depicted in Figure 3 which shows unsteady Mach contours for selected time-steps including subsonic flow during start-up, the transition to supersonic flow, steady-state operation, and the shut-down sequence. During start-up, the inlet pressure is initially very small, the flow is over-expanded, and free boundary shock reflection occurs as can be seen in Figure 3 for $t \leq 0.30ms$.

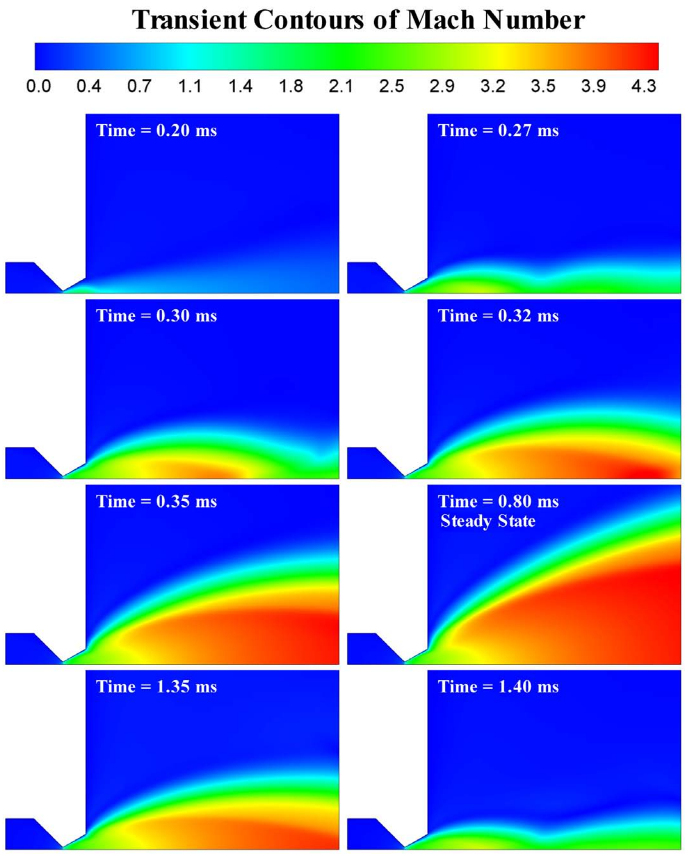

FIGURE 3. The plume sequence during a single micronozzle duty cycle as shown by contours of Mach number.

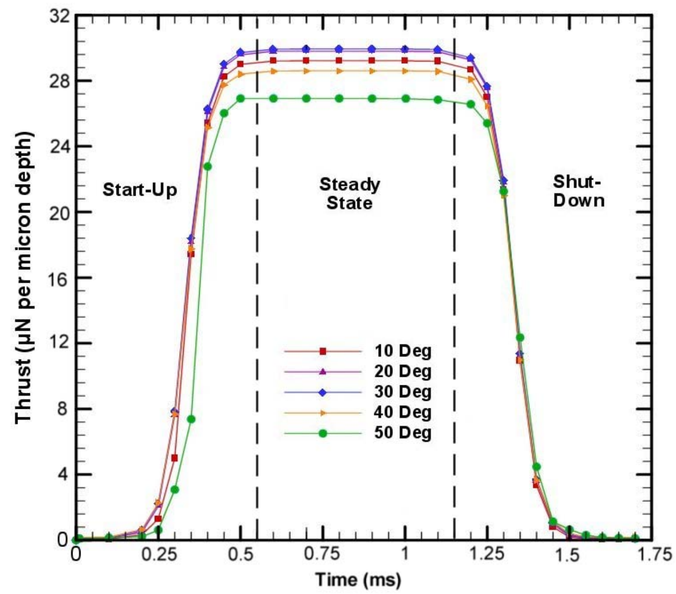

FIGURE 4. The transient thrust profile for $2D$ micronozzles with varying expander half-angles from $10° - 50°$.

As time increases during the duty cycle, the inlet pressure, mass flow rate (Eq. (11)), and size of the exhaust plume increase accordingly. During this process the flow-field transitions from over-expanded $t < 0.32ms$, through perfectly expanded flow at $t = 0.32ms$, and finally to under-expanded exit flow where an expansion fan develops at the nozzle exit. The steady-state portion of the duty cycle is denoted by an inlet pressure that is 99% of the steady-state inlet stagnation pressure of $250kPa$. This occurs during the time range of $0.55ms - 1.15ms$ and the steady-state flow-field is shown in Figure 3 represented by the time $t = 0.8ms$. The flow response and flow-field characteristics are well explained by conventional gas dynamics and depict expected nozzle flow and plume behavior. During the shut-down process of the thruster duty cycle, the start-up sequence and nozzle flow behavior is essentially repeated but in reverse order.

It should be noted that flow-field details may be less accurate far downstream of the nozzle exit plane and in the exhaust plume owing to rarefaction effects that are not accounted for with a continuum model. In designing a supersonic thruster nozzle, the level of accuracy required in the modeling of the plume region is really a matter of interest. For example, if the interest lies in the chemical signatures of the exhaust plume or perhaps the interaction of the plume with a spacecrafts solid surfaces, then flow rarefaction cannot be ignored. On the other hand, if thrust production by the nozzle is the key item of interest, as is the case for this work, then the specifics of the supersonic plume are of no real import. As such, any model inaccuracies accrued within the exhaust plume *do not* affect thrust and performance calculations as the flow remains in the continuum regime at the nozzle exit (where thrust is calculated) and so the focus and approach of this study remain valid.

Thrust results as a function of time have been calculated as per Eq. (10) for expander half-angles of$10° - 50°$. The axial thrust output of the micronozzle has been determined in units of micro-Newtons per micron depth of the thruster. The thrust profiles during the actuation cycle are shown in Figure 4. A close-up view of the thrust profile during start-up and shut-down can be seen on the left and right of Figure 5, respectivley. All of the expanders exhibit some degree of thrust 'lag' in response to the increasing inlet pressure profile - a direct consequence of viscous effects. This lag is most pronounced in the $10°$ and $50°$ expanders as these half-angles exhibit the largest subsonic layer growth as previously shown in Ref [20]. As the pressure ratio across the nozzle is increased, the flow must overcome viscous forces and push aside the subsonic layer in order to allow the flow to undergo supersonic expansion and generate thrust. Similarly, there is a distinct difference in performance once steady-state is

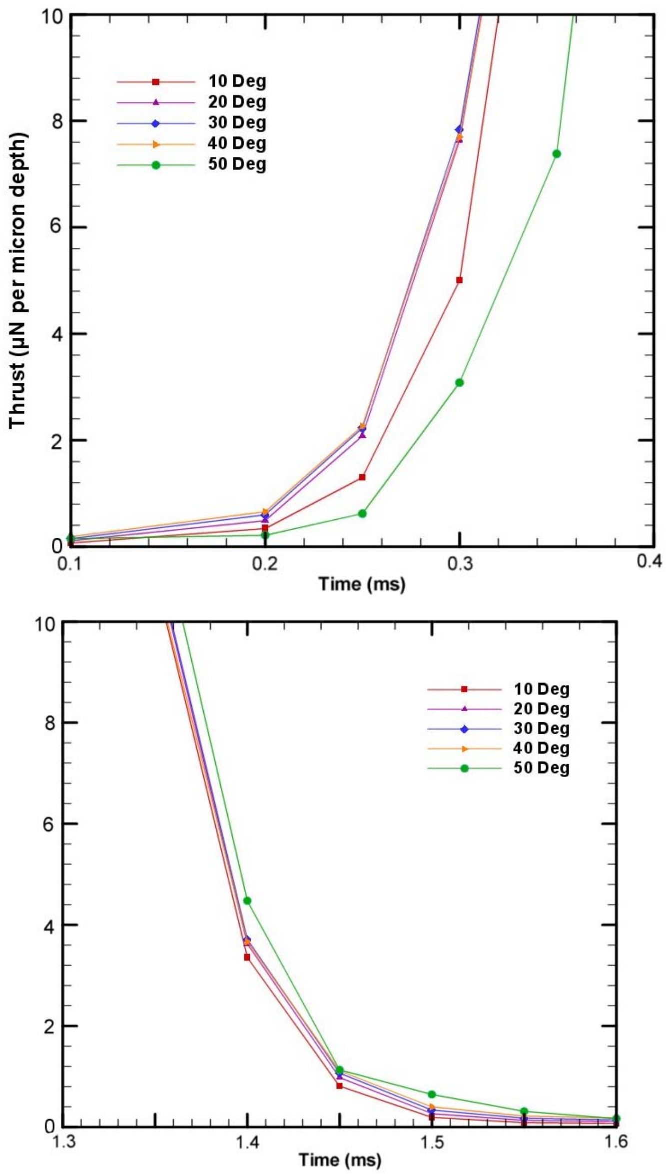

FIGURE 5. A close-up view of the start-up and shut-down thrust profiles. Note the lag during start-up that is not observed during shut-down.

achieved that depends on the expander angle. During the shut down process, viscous forces facilitate the thrust response by reducing flow as the inlet pressure decreases during valve closure. All of the half-angles exhibit similar a nearly identical response to valve closure.

The total impulse and impulse efficiency have been calculated according to Eq.s (11) and (12), respectively, and the results are shown in Figure 6. Here we see that the 30° expander exhibits maximum performance impulse and efficiency. As such, we will focus our attention on $3D$ micronozzles with 30° expander half-angles.

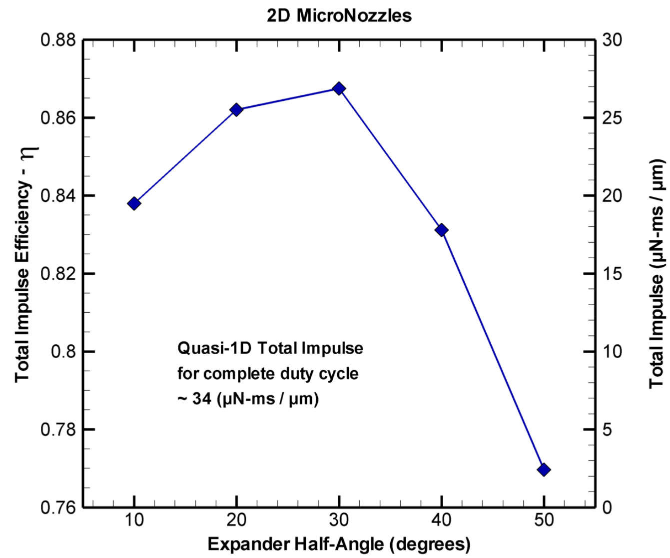

FIGURE 6. he total impulse produced in $2D$ micronozzles for the complete duty cycle. The 30° expander exhibits the greatest efficiency. The drop off in efficiency for large expader angles is a result of transverse velocity components associated with a large divergence angle. The decreases in performance at small exapnder angles is due to viscous effects.

3D Results

As an illustration of the flow-field in a $150\mu m$ deep nozzle, $3D$ Mach number contours in the micronozzle and exhaust plume are shown in Figure 7 for actuation time $t = 0.6ms$ $(Re \sim 800)$. The $3D$ subsonic layer growth in the expander is shown in Figure 8 at selected locations at time $t = 0.27ms$ $(Re \sim 30)$. Note that the relatively low Reynolds results in a subsonic layer that occupies a significant portion of the expander. However, the central core of the flow is supersonic.

A common measure of the influence of viscous forces is the portion of the exit plane occupied by the subsonic layer. At very low inlet pressures (Re) associated with early start-up and late shut-down, viscous forces cause the entire exit plane of the micronozzle to be subsonic - significantly reducing performance. At the higher Reynolds numbers associated with the steady-state portion of the duty cycle, the subsonic layer occupies only a fraction of the exit plane. As such, we wish to characterize the temporal evolution of the subsonic layer.

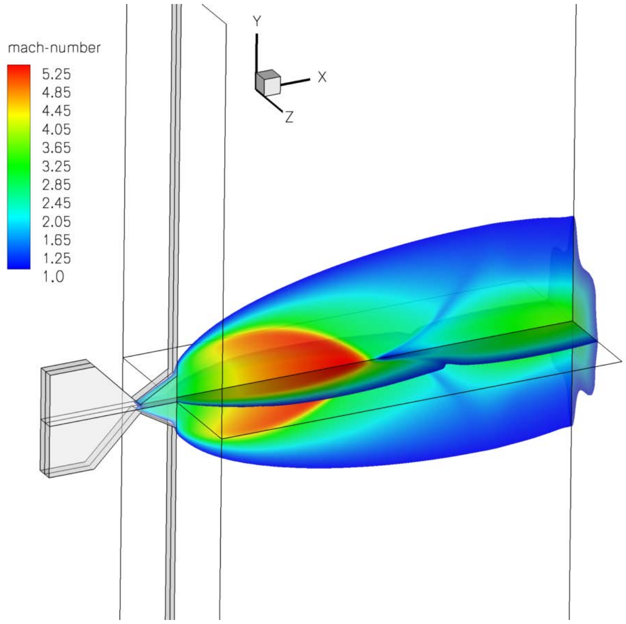

FIGURE 7. An illustration of the steady-state ($Re \sim 800$), 3D Mach number contours in a $150\mu m$ deep nozzle and exhaust plume.

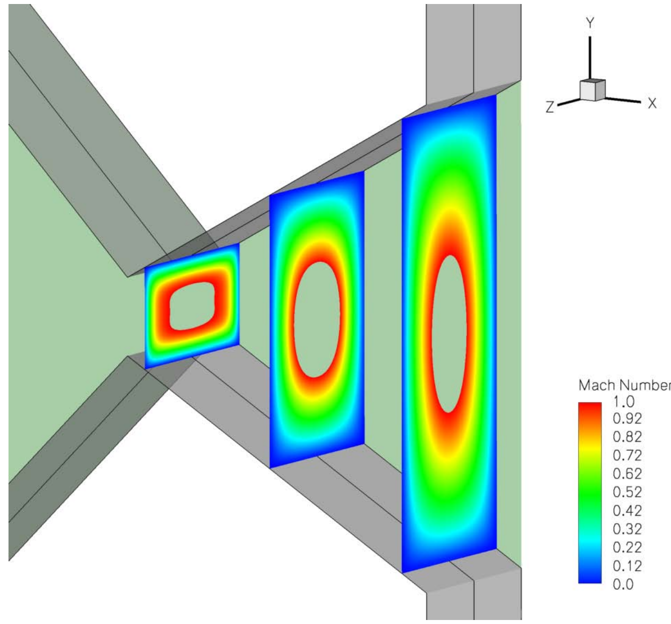

FIGURE 8. The subsonic layer in a 50 micron deep micronozzle operating at $Re \sim 30$.

In Figures 9 and 10 we see the subsonic layer at the micronozzle exit plane, denoted by Mach contours $M < 1$, in the $150\mu m$ and $100\mu m$ deep nozzles, respectively, for time steps that capture the transition from a completely subsonic exit to the steady-state condition. For the $150\mu m$ deep nozzle, the transition begins at $t = 0.22ms$ $(p_0 = 9.5kPa, Re \sim 30)$ while for the $100\mu m$ deep nozzle the transition begins at $t = 0.25ms$ $(p_0 = 20.4kPa, Re \sim 65)$. While not shown in a figure, we mention here that for the $50\mu m$ deep nozzle the transition beins at $t = 0.27ms$ $(p_0 = 33.8kPa, Re \sim 106)$. The trend shown here is that a shallow nozzle requires a longer time period during start-up, or equivalently a greater inlet pressure (Re), in order to over come viscous forces and produce a supersonic exit condition. In general, a shallow nozzle experiences greater viscous forces and thus increased viscous losses.

The influence of viscous forces and the susonic layer manifest themselves by causing a flow-response lag and reduced nozzle performance. Figure 11 shows the thrust profiles as a function of time during the first half of the duty cycle $(0.8ms)$ for the four nozzle depths of interest. For comparison, thrust results are presented as a per unit depth basis and the quasi-1D profile which responds instantly to valve acuation is also shown. Figure 11 shows that all nozzles exhibit a 'lag' in thrust response with the $25\mu m$ deep nozzle having the greatest delay. The response time improves as the depth increases. Similarly, the thrust produced per unit depth increases with nozzle depth.

The total impulse produced during start-up (i.e., the first $0.55ms$ of the duty cycle) is plotted in Figure 12 along with the impulse efficiency. The $\mathbf{I}_{\max}$ calculated according to quasi-1D theory is ~ 7.6 $(\mu N \cdot ms/\mu m)$. Here it is seen that the impulse efficiency increases with depth and approaches the $2D$ results for sufficiently deep micronozzles. The maximum impulse efficiency during start-up is 0.7 for the $150\mu m$ deep nozzle while a minimum efficiency of 0.22 is observed for the $25\mu m$ deep nozzle.

CONCLUSIONS

In this study we have described an ongoing project aimed at better understanding the interplay of nozzle geometry and viscous effects for the transient operation of a supersonic micronozzle. Our goal has been to characterize transient micronozzle flow and performance via the simulation of a realistic microvalve duty cycle utilizing a H_2O_2 monopropellant scheme. We have sought to delineate the thrust production as a function of time, the total impulse delivered during a single firing, and determine nozzle impulse efficiencies based on theoretical maximum performance. The specific contributions of this work include detailed examinations of the following: (1) a $3D$ transient supersonic micronozzle flow analysis based on a realistic valve duty cycle, (2) variable nozzle depths from $25 - 150\mu m$, (3) and the simulation of decomposed H_2O_2 monopropellant.

The numerical results indicate that a 'lag' in flow response and thrust production exists during start-up for all cases examined. This lag is especially pronounced for cases with relatively large viscous forces, i.e., shallow 3*D* micronozzles or micronozzles with extremely large (50°) or small (10°) expander half-angles. Support for this conclusion is observed in the subsonic layer behavior at the nozzle exit plane. A response delay is not observed during shut-down as viscous forces act to reduce flow and facilitate the shut-down response.

It is found that the maximum impulse delivered and maximum impulse efficiency is achieved for a 3*D* micronozzle with an expander half-angle of 30°. This result is consistent with previous 2*D* simulations. It is worthy of note that this value is approximately ($2\times$) the typical half-angle used in macro-scale conical thrusters.

ACKNOWLEDGMENT

This work was supported by the U.S. Air Force Office of Sponsored Research (AFOSR) under Grant # FA9550-06-1-0364.

REFERENCES

[1] Helvajian, H and Janson, S W *Small Satellites: Past, Present, and Future*, The Aerospace Press (AIAA), El Segundo, CA, 2008.

[2] R.L. Bayt, and K.S. Breuer 1998 "Viscous Effects in Supersonic MEMS-based Micronozzles" Proc. 3rd ASME Microfluids Symp. (Anaheim, CA).

[3] R.L. Bayt, and K.S. Breuer, "System design and performance of hot and cold supersonic microjets," AIAA Paper 2001-0721, 2001.

[4] Alexeenko A A, Levin D A, Gimelshein S F, and Collins R J 2000 "Numerical Modeling of Axisymmetric and Three-Dimensional Flows in MEMS Nozzles" Proc. 36th AIAA/ASME/SAE/ASEE Joint Propulsion Conf. Exhibit (Huntsville, Al).

[5] Alexeenko A A, Levin D A, Gimelshein S F, Collins R J, and Reed B D 2001 "Numerical Modeling of Axisymmetric and Three-Dimensional Flows in Microelectromechanical Systems Nozzles" AIAA Journal Vol. 40, No. 5 May 2002 pp. 897-904.

[6] Alexeenko A and Levin D, "Numerical Simulation of High-Temperature Gas Flows in a millimeter-Scale Thruster," Journal of Thermophysics and Heat Transfer, 16 No. 1, 2002.

[7] Alexeenko, A A, Gimelshein, S.F., Levin, D.A., Ketsdever, A.D., and Ivanov, M.S., "Measurements and Simulation of Orifice Flow for Micropropulsion Testing," J. of Propulsion and Power, Vol. 19, No. 4, July 2003.

[8] Alexeenko, A A , Levin, D A, Fedosov, D.A., Gimelshein, S.F., and Collins, R.J. "Performance Analysis of Microthrusters Based on Coupled Thermal-Fluid Modeling and Simulation." J. of Propulsion and Power. Vol. 21, No. 1, 2005.

[9] Alexeenko, A A, Fedosov, D A, Gimelshein, S.F., Levin, D.A., and Collins, R.J. "Transient Heat Transfer and Gas Flow in a MEMS-Based Thruster" J. of MEMS. Vol. 15, No 1, 2006.

[10] Ketsdever A D, Clabough M T., Gimelshein S F., and Alexeenko A. "Experimental and Numerical Determination of Micropropulsion Device Efficiencies at Low Reynolds Numbers." AIAA Journal Vol. 43, No. 3 March 2005.

[11] Louisos, W F & Hitt, D L "Viscous Effects in Supersonic Micro-Nozzle Flows: Transient Analysis," Proc. 36th AIAA Fluid Dynamics Conference, June 5-8 2006, San Francisco, California. Paper No. AIAA-2006-2874.

[12] Kujawa J. and Hitt D.L., 2004, "Transient Shutdown Simulations of Realistic MEMS Supersonic Nozzles" AIAA Paper 2004-3762

[13] Morinigo, J.A., Quesada, J H "Analysis of Viscous Heating in a Micro-Rocket Flow and Performance" Journal of Thermal Science, Vol. 17, No. 2, 2008.

[14] D.L. Hitt, C. Zakrzwski and M. Thomas, "MEMS-Based Satellite Micropropulsion Via Catalyzed Hydrogen Peroxide Decomposition," J. Smart Mater and Struct., Volume 10, pp. 1163-1175, 2001.

[15] Kwang W Oh and Chong H Ahn "A Review of Microvalves." J. of Micromechanics and Microengineering. Issue 5, May 2006.

[16] Mueller, J., Marrese, C., Polk, J., Yang, E., Green, A., White, V., Bame, D., Chakraborty, I., Vargo, S., and Reinicke, R. "An Overview of MEMS-Based Micropropulsion Developments at JPL." J. of International Academy of Astronautics. May, 2003.

[17] McBride, B. and Sanford, G. *NASA-Glenn Chemical Equilibrium Program* CEA2, NASA RP-1311, Part I, 1994 and NASA RP-1311, Part II, 1996.

[18] Vargaftik, N.B., *Thermophysical Properties of Gases and Liquids, 2nd ed.*, Hemisphere Publishing, New York, 1975.

[19] Anderson, John D. Jr. *Modern Compressible Flow with Historical Perspective*. Edition 3, McGraw-Hill, Boston, MA, 2003.

[20] Louisos, WF. and Hitt, DL "Viscous Effects on Performance of 2D Supersonic Linear micronozzles" AIAA Journal of Spacecraft and Rockets, Vol. 45, No. 4, 2008. p. 706.

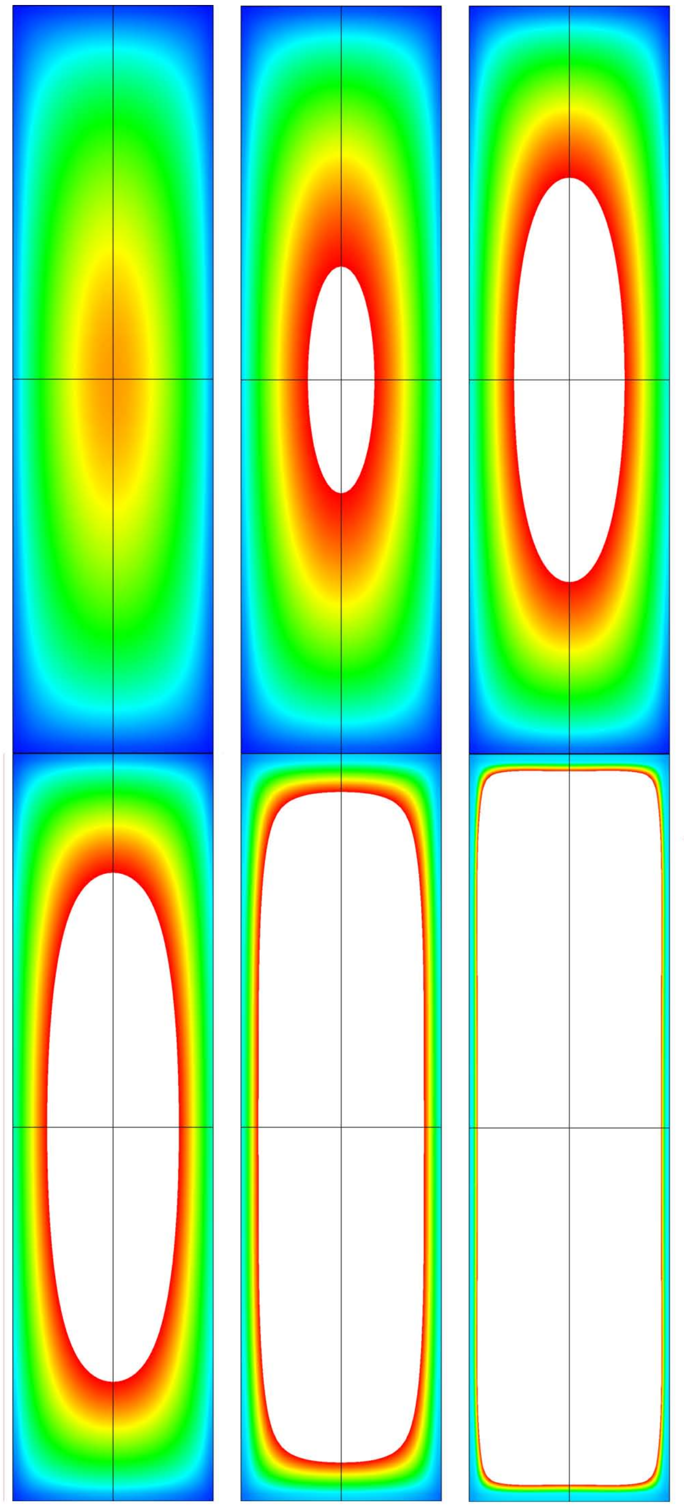

FIGURE 9. The subsonic layers at the micronozzle exit plane in the $150\mu m$ deep micronozzle shown for increasing times during start-up of 0.22, 0.23, 0.24, 0.25, 0.3, and $0.8ms$.

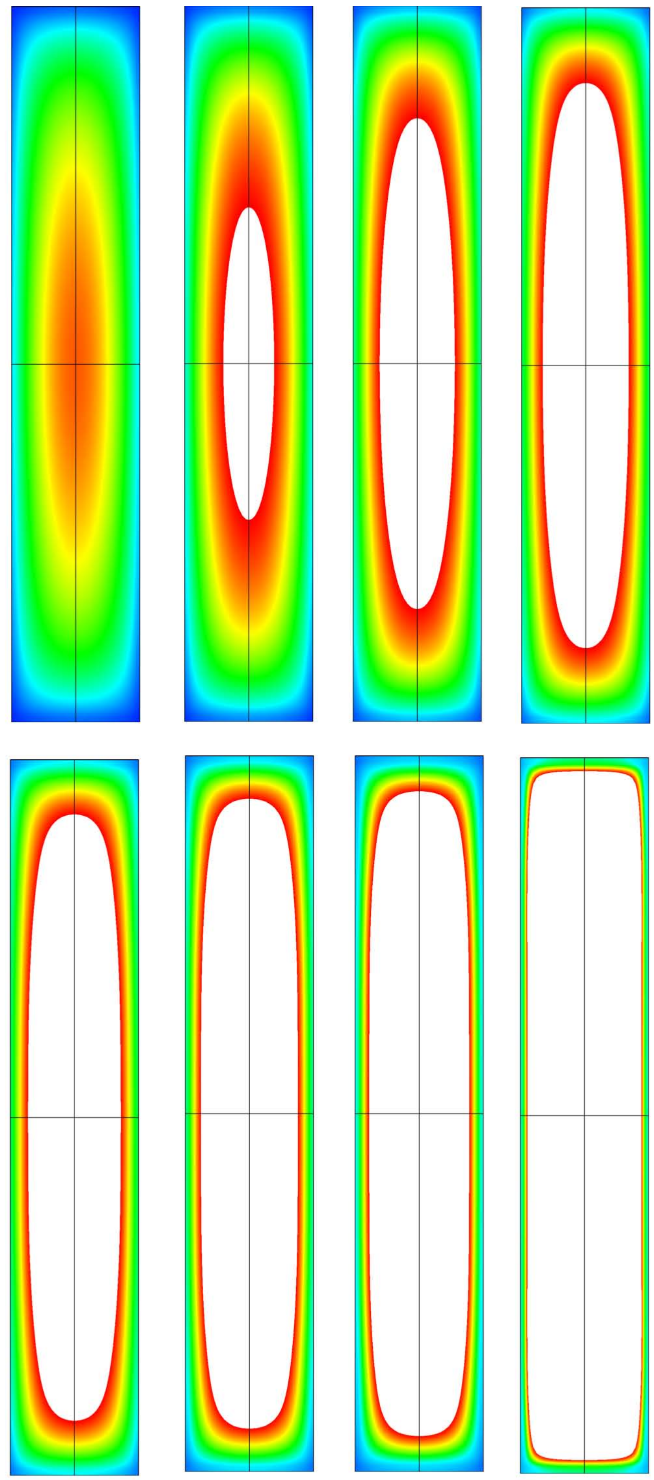

FIGURE 10. he subsonic layers at the micronozzle exit plane in the $100\mu m$ deep micronozzle shown for increasing times during start-up of 0.24, 0.25, 0.26, 0.27, 0.28, 0.29, 0.3, and $0.8ms$.

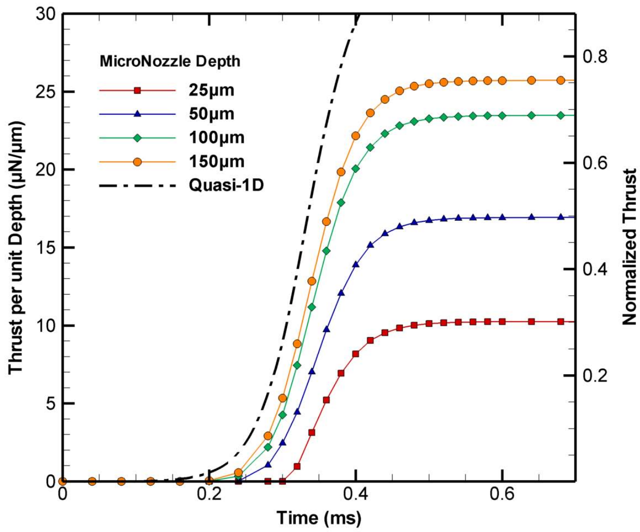

FIGURE 11. The 3*D* thrust profiles during start-up for the four micronozzle depths of interest. For comparison purposes, thrust results are shown per unit depth as well as normalized by quasi-1D theory.

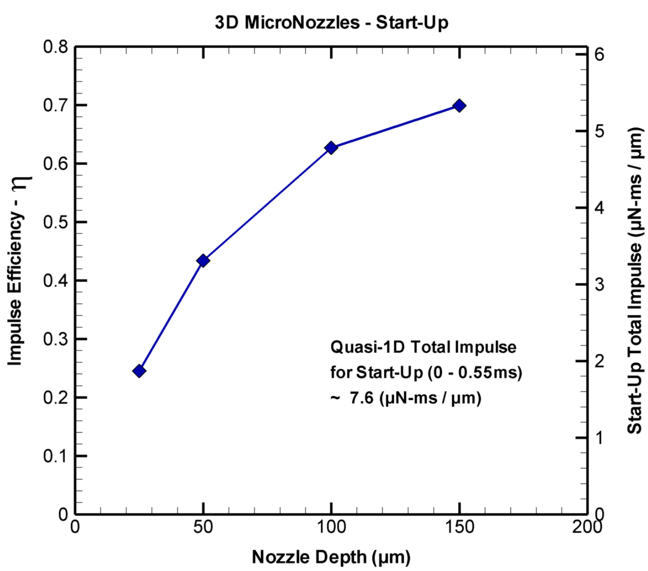

FIGURE 12. The impulse efficiency and total impulse generated by 3*D* micronozzles during the thruster start-up sequence of the duty cycle, i.e., for time $0-0.55ms$.